RSC Applied Interfaces

ROYAL SOCIETY OF CHEMISTRY

PAPER

View Article Online
View Journal | View Issue

Check for updates

Cite this: *RSC Appl. Interfaces*, 2025, **2**, 795

Conductive RuO_2 binders enhance mechanical stability of macroporous Nb–SnO_2 particles as cathode catalyst supports for high-performance PEFCs†

Thi Thanh Nguyen Ho,[a] Tomoyuki Hirano, *[a] Aoi Takano,[b] Syu Miyasaka,[b] Eishi Tanabe,[c] Makoto Maeda,[d] Eka Lutfi Septiani,[a] Kiet Le Anh Cao[a] and Takashi Ogi *[a]

Niobium-doped tin oxide (NTO) particles with a macroporous structure have been developed as catalyst supports for enhancing the durability and performance of polymer electrolyte fuel cells (PEFCs). This macroporous architecture improves the mass transport properties of the electrode. However, their weak mechanical strength can cause structural collapse, thereby limiting single-cell performance at high current densities. In this study, we employed ruthenium oxide (RuO_2) as a binder to integrate with macroporous NTO particles (denoted as NTO/RuO_2). This approach simultaneously enhanced the electrical conductivity and mechanical strength of the catalyst supports, improving the performance of PEFCs. Incorporating RuO_2 binders effectively stabilized the macroporous structure, and the NTO/RuO_2 particles with 50 wt% RuO_2 loading maintained their structural integrity under high compression pressures of up to 40 MPa. The aggregated NTO/RuO_2 particles containing 50 wt% RuO_2 binder also exhibited higher conductivity than the NTO aggregates without RuO_2 binder, which was attributed to the conductive network formed by RuO_2. Importantly, the membrane electrode assembly (MEA) fabricated with macroporous NTO/RuO_2 particles containing 20 wt% RuO_2 binder achieved a maximum current density of 2.16 A cm^{-2} at 60 °C and 100% relative humidity (RH), outperforming the MEA utilizing Carbon Vulcan as the support (2.06 A cm^{-2}). Furthermore, the enhanced hydrophilic properties of the RuO_2 binder improved water retention at the catalyst layer/membrane interface, thus promoting membrane hydration and overall cell performance at a high temperature of 80 °C and a low RH of 30%.

Received 5th December 2024,
Accepted 18th March 2025

DOI: 10.1039/d4lf00404c

rsc.li/RSCApplInter

Open Access Article. Published on 24 March 2025. Downloaded on 6/13/2026 6:29:26 PM.
This article is licensed under a Creative Commons Attribution 3.0 Unported Licence.

Introduction

In recent years, polymer electrolyte fuel cells (PEFCs) have attracted significant attention as environmentally friendly devices for energy storage and conversion,[1–4] with increasing applications in heavy-duty vehicles, such as trucks, buses, and ships.[5,6] Carbon is a conventional catalyst support for PEFCs owing to its excellent electrical conductivity, high surface area, and suitable pore structure.[7–10] However, these carbon materials are prone to corrosion in the highly corrosive environments associated with PEFC operation, resulting in a decline in both performance and durability.[7,11] To address this challenge, metal oxide nanoparticles with improved corrosion resistance have been developed as promising support materials to replace traditional carbon in fuel cell electrodes.[12–15]

Niobium-doped tin oxide (NTO) nanoparticles have demonstrated great potential as cathode catalyst supports in PEFCs owing to their high electrical conductivity and

[a] *Chemical Engineering Program, Graduate School of Advanced Science and Engineering, Hiroshima University, 1-4-1 Kagamiyama, Higashihiroshima, Hiroshima 739-8527, Japan. E-mail: tomoyuki-hirano@hiroshima-u.ac.jp, ogit@hiroshima-u.ac.jp; Tel: +81 82 424 7850, +81 82 424 3765*
[b] *Cataler Corporation, 7800 Chihama, Kakegawa, Shizuoka 437-1492, Japan*
[c] *Hiroshima Prefectural Institute of Industrial Science and Technology, 3-10-31 Kagamiyama, Higashi Hiroshima, Hiroshima 739-0046, Japan*
[d] *Natural Science Center for Basic Research and Development, Hiroshima University, 1-4-1 Kagamiyama, Higashihiroshima, Hiroshima 739-8527, Japan*

† Electronic supplementary information (ESI) available: Figure showing SEM images of macroporous NTO/RuO_2-50 particles synthesized with different PMMA concentrations and STEM images of macroporous RuO_2/NTO particles. A table showing a summary of specific surface areas of macroporous NTO/RuO_2 particles. Figure showing BET nitrogen adsorption isotherm plots of NTO nanoparticles and macroporous NTO/RuO_2 particles. Table presenting crystallographic parameters of RuO_2, Ru, and SnO_2 derived from XRD refinement of macroporous NTO/RuO_2 particles. Figure presenting the XRD pattern, TEM image and size distribution chart of NTO nanoparticles. Figure showing the cyclic voltammograms of carbon, NTO nanoparticles, and macroporous NTO/RuO_2 particles with varying RuO_2 binder contents before and after durability tests. See DOI: **https://doi.org/10.1039/d4lf00404c**

© 2025 The Author(s). Published by the Royal Society of Chemistry

Open Access Article. Published on 24 March 2025. Downloaded on 6/13/2026 6:29:26 PM. This article is licensed under a Creative Commons Attribution 3.0 Unported Licence.

exceptional corrosion resistance.[16,17] Kakinuma *et al.* reported that NTO nanoparticles with a dopant concentration of 4.0% exhibited higher electrical conductivity than Nb-free SnO_2. Furthermore, the cells with Pt/NTO cathodes showed better performance and durability than those with Pt/carbon black cathodes when operated at potentials above 0.4 V.[16] Our research group also synthesized NTO nanoparticles using flame spray pyrolysis and evaluated their performance as PEFC cathode catalyst supports.[17–19] The flame-made NTO nanoparticles formed a fused aggregate network structure *via* a combustion reaction during synthesis, which reduced the interparticle resistance between oxide nanoparticles and enhanced conductivity. Nevertheless, compared to traditional carbon supports, oxide supports generally have lower porosity and less developed structures, which continue to present challenges for achieving high power generation performance.

A potential solution to this problem is to employ support particles with macroporous structures. Our group reported the synthesis of macroporous particles by a template-assisted aerosol process,[20–25] which had been extensively utilized for producing macroporous structures in a wide range of materials.[20,22,26,27] The high porosity of macroporous supports provides accessible pores, promoting the diffusion of reactants and products.[21,28–31] Faustini *et al.* synthesized an iridium-based catalyst with an ultraporous hierarchical structure *via* spray drying, which proved to be an effective catalyst for proton exchange membrane water electrolysis.[28] The macroporous structure of $Ir_{0.7}Ru_{0.3}O_2$ ultraporous spheres created an effective electron-conducting pathway throughout the catalyst layer, while the high porosity improved gas and water transport.

In our previous report, we demonstrated that using a 300 nm poly(methyl methacrylate) (PMMA) template to prepare macroporous NTO particles could enhance their performance as catalyst supports in single cells.[32] However, under the high pressure of membrane electrode assembly (MEA) fabrication, the macropore framework of the NTO particles collapsed due to their poor mechanical strength, decreasing the porosity of the catalyst layer. Therefore, a macroporous NTO catalyst support with a mechanically stable structure is desirable to achieve high-performance cathode catalysts for PEFCs.

Many studies have used binders to improve the mechanical strength of porous frameworks[33–35] and investigated their functions in the fabrication processes. These studies collectively highlight the efficacy of binders in enhancing the mechanical strength of porous materials. Motivated by this concept, we applied binders in this study to improve the mechanical strength of macroporous NTO particles. Considering that insulator binders can increase the contact resistance between active materials, resulting in reduced PEFC performance, conductive binders are essential to strengthen the macroporous frameworks for achieving high-performance PEFCs. Ruthenium oxide (RuO_2) is known as a metallic conductor with an electrical conductivity of 2.0×10^4 S cm^{-1} at 28 °C, which decreases at lower temperatures.[36,37] Additionally, RuO_2–SnO_2 is utilized in various electrochemical applications, such as supercapacitors, chlorine evolution, and water electrolysis.[38,39] Using RuO_2 as a binder to combine with NTO particles is expected to not only reinforce the structural integrity of the macroporous framework but also enhance its electrical conductivity. Therefore, to design a suitable catalyst support, it is crucial to understand the effect of binder introduction on the mechanical properties and electrical conductivity of the macroporous structure, as well as its impact on PEFC performance. It is also important to determine the effects of various concentrations of RuO_2 binder on the mechanical strength of the macroporous structure and the overall PEFC performance. To the best of our knowledge, macroporous NTO/RuO_2 particles have not been reported as catalyst supports for PEFCs.

In this study, we designed a cathode catalyst support using NTO/RuO_2 particles with macroporous structures prepared by flame-assisted spray pyrolysis (FASP). In the FASP process, the presence of liquid- and vapor-phase precursors allows for better control over particle morphology and structure.[15,40–48] In addition, this method has been scaled up for industrial use in the production of fine particles.[49,50] The effect of RuO_2 binder contents on the structure and morphology of the macroporous NTO/RuO_2 particles was investigated. The electrical conductivity of the NTO/RuO_2 particle was also examined. Importantly, the mechanical strength of the macroporous structure of NTO/RuO_2 particle with different RuO_2 binder contents was also evaluated. Eventually, the performance of MEAs using macroporous NTO/RuO_2 particles as cathode catalyst support was performed under both low and high relative humidity conditions.

Results and discussion

Preparation of macroporous NTO/RuO_2 particles

RuO_2 and SnO_2 share several structural similarities, enabling the facile formation of a RuO_2–SnO_2 composite, which is crucial for creating a robust macroporous framework. Assisted by these features, macroporous NTO/RuO_2 particles with different contents of RuO_2 binder (0 to 50 wt%) were synthesized using FASP, followed by annealing to completely remove the PMMA template. Fig. 1A depicts the synthesis workflow, starting with the FASP of mechanically stable macroporous NTO particles templated with PMMA and bound by RuO_2 (NTO/RuO_2). In the absence of RuO_2 binders, NTO nanoparticles and PMMA templates were dispersed in water to form a precursor solution, and macroporous particles were produced through a conventional template-assisted spray pyrolysis process. In contrast, macroporous NTO/RuO_2 particles were obtained using a precursor solution consisting of $RuCl_3$ salt, PMMA templates, and NTO nanoparticles. In this process, $RuCl_3$ salt decomposes under high-temperature conditions to form RuO_2 as a binder in the gaps between NTO nanoparticles within the precursor droplets in the gas phase. Additionally, the precipitation of RuO_2 between NTO nanoparticles results in the formation of a conductive network in the structure, improving the electrical conductivity of the macroporous NTO/RuO_2 particles. Since the short residence time and rapid cooling in the FASP process,[51–53]

© 2025 The Author(s). Published by the Royal Society of Chemistry

Open Access Article. Published on 24 March 2025. Downloaded on 6/13/2026 6:29:26 PM.
This article is licensed under a Creative Commons Attribution 3.0 Unported Licence.

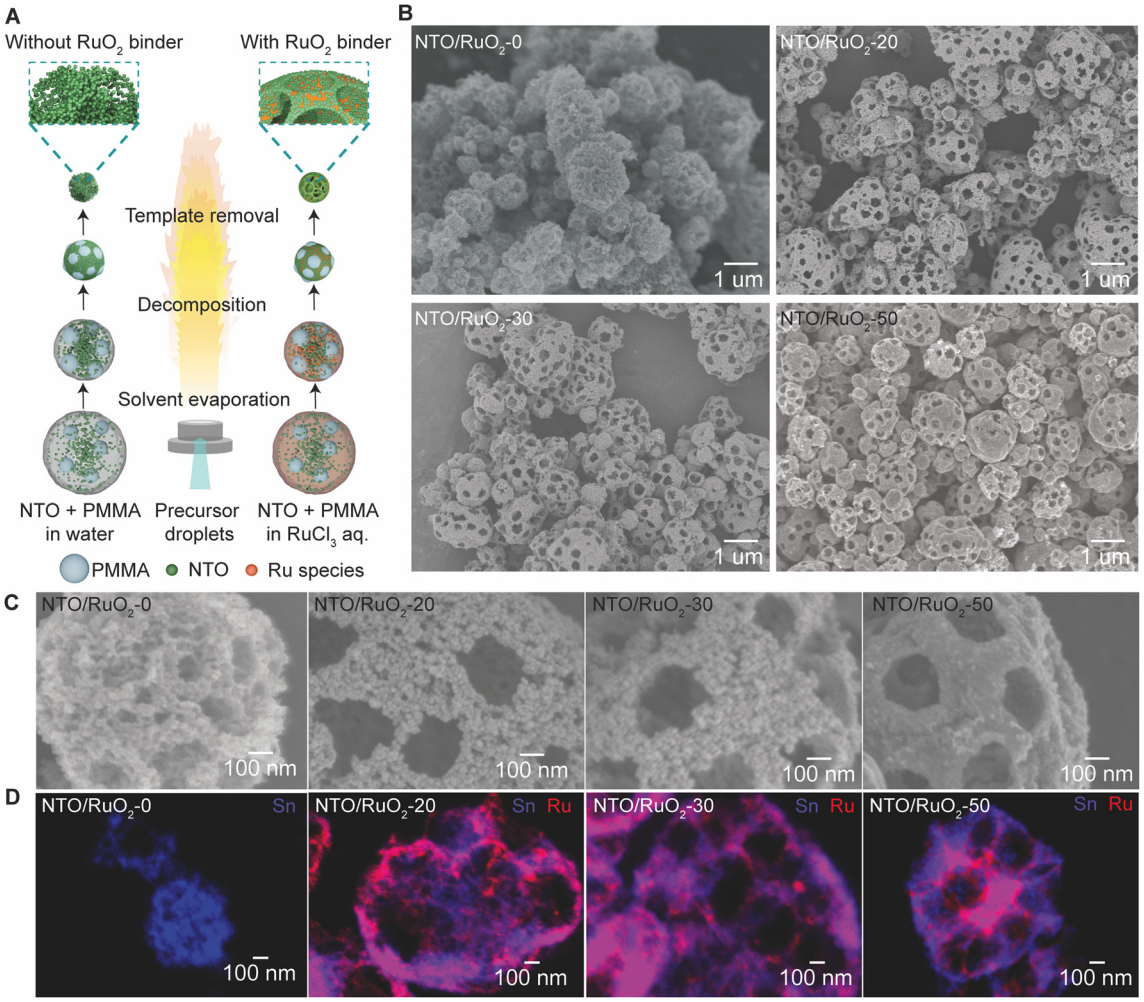

Fig. 1 (A) Synthesis workflow starting with the FASP of mechanically stable macroporous NTO particles, templated by PMMA, and bound by RuO_2, (B) SEM images of macroporous NTO/RuO_2 particles prepared with different RuO_2 binder concentrations, (C) high-magnification SEM images focusing on the surface of macroporous NTO/RuO_2 particles synthesized with varying concentrations of RuO_2 binder, and (D) energy-dispersive X-ray spectroscopy mapping for Sn (purple) and Ru (red), demonstrating that the RuO_2 binder was distributed throughout the entire structure of macroporous NTO/RuO_2 particles.

the decomposition of the PMMA template was incomplete. Therefore, a post-annealing treatment was performed to fully remove the remaining PMMA template and achieve the desired macroporous structure of NTO/RuO_2 particles.

The morphology of the macroporous NTO/RuO_2 particles was examined using scanning electron microscopy (SEM). The influence of PMMA template concentration (0 to 2.0 wt%) on the structure of the macroporous NTO/RuO_2 particles was investigated when the RuO_2 binder concentration was fixed at 50 wt%. As shown in the SEM images (Fig. S1†), increasing the PMMA concentration resulted in more open macropores on the particle surfaces. However, at 2.0 wt%, the template concentration was too high, causing the macroporous framework to collapse. Therefore, a PMMA template concentration of 1.0 wt% was selected for subsequent experiments to ensure a robust macropore framework and ample open macropores. Fig. 1B shows the SEM images of the macroporous NTO/RuO_2 particles prepared with different RuO_2 binder concentrations, wherein well-developed macropores were derived from PMMA templates in the presence of RuO_2 binders. Fig. 1C shows the magnified SEM images of the particle surfaces. The macroporous NTO/RuO_2-0 particles (without RuO_2) exhibited spherical shapes with rough surfaces formed from aggregated NTO nanoparticles. Notably, significant voids were observed between aggregated NTO nanoparticles, and this relatively high void fraction within the macropore framework could compromise the mechanical strength. It is important to note that the mechanical stability of a porous structure is largely determined by its framework porosity – the void fraction within the macropore framework – as highly porous structures typically exhibit weak mechanical strength.[54] Upon the addition of RuO_2 binders at concentrations of 20 wt% (NTO/RuO_2-20) and 30 wt% (NTO/RuO_2-30), the macropore frameworks were more distinct, and the particle surfaces became smoother. As the concentration of RuO_2 continued to increase, the macropore framework persisted, and the number of broken particles

Open Access Article. Published on 24 March 2025. Downloaded on 6/13/2026 6:29:26 PM.
This article is licensed under a Creative Commons Attribution 3.0 Unported Licence.

considerably decreased. The surfaces of the NTO/RuO_2-50 particles (50 wt% RuO_2) became slicker, and the number of voids between NTO nanoparticles decreased significantly. The porosity of the framework, which is the percentage of voids between NTO nanoparticles, was reduced by the incorporation of the RuO_2 binder. The RuO_2 binder effectively filled the voids, strengthening the structural connectivity and significantly enhancing the mechanical stability of the macroporous framework. The scanning transmission electron microscopy (STEM) images (Fig. S2†) also confirmed the porosity reduction in the framework with the increasing RuO_2 concentration. As shown in Table S1 and Fig. S3,† the incorporation of RuO_2 binder reduced the specific surface area of the macroporous NTO/RuO_2 particles. Specifically, the specific surface areas calculated using the BET equation were 106.9 $m^2\ g^{-1}$ and 71.1 $m^2\ g^{-1}$ for NTO nanoparticles and macroporous NTO/RuO_2-0 particles, respectively. The lower specific surface area of NTO/RuO_2-0 is attributed to the aggregation of NTO nanoparticles during the flame process and the annealing treatment to remove PMMA templates. The specific surface area of the macroporous NTO/RuO_2 particles further decreased with the increasing RuO_2 binder concentration, reaching 30.4 $m^2\ g^{-1}$ for NTO/RuO_2-50. These results confirm a decrease in the framework porosity with the increasing RuO_2 binder content. The energy-dispersive X-ray (EDX) elemental mapping in Fig. 1D shows that the RuO_2 binder distributes uniformly within the entire structure of the macroporous particles. During the self-organization process of precursor droplets floating in the flame, Ru species, which are smaller than NTO nanoparticles and PMMA templates, experience lower buoyancy and higher Brownian motion, allowing them to move more easily and fill the spaces between the larger particles.[55–57] Additionally, RuO_2 species nucleated and precipitated onto the surface of NTO nanoparticles, reducing voids between NTO nanoparticles during the assembly process. This self-organization leads to the distribution of RuO_2 throughout the particles, which is expected to increase the framework density and enhance the mechanical durability of the macroporous particles.

Fig. 2A shows the X-ray diffraction (XRD) patterns of the macroporous NTO/RuO_2 particles with different RuO_2 binder

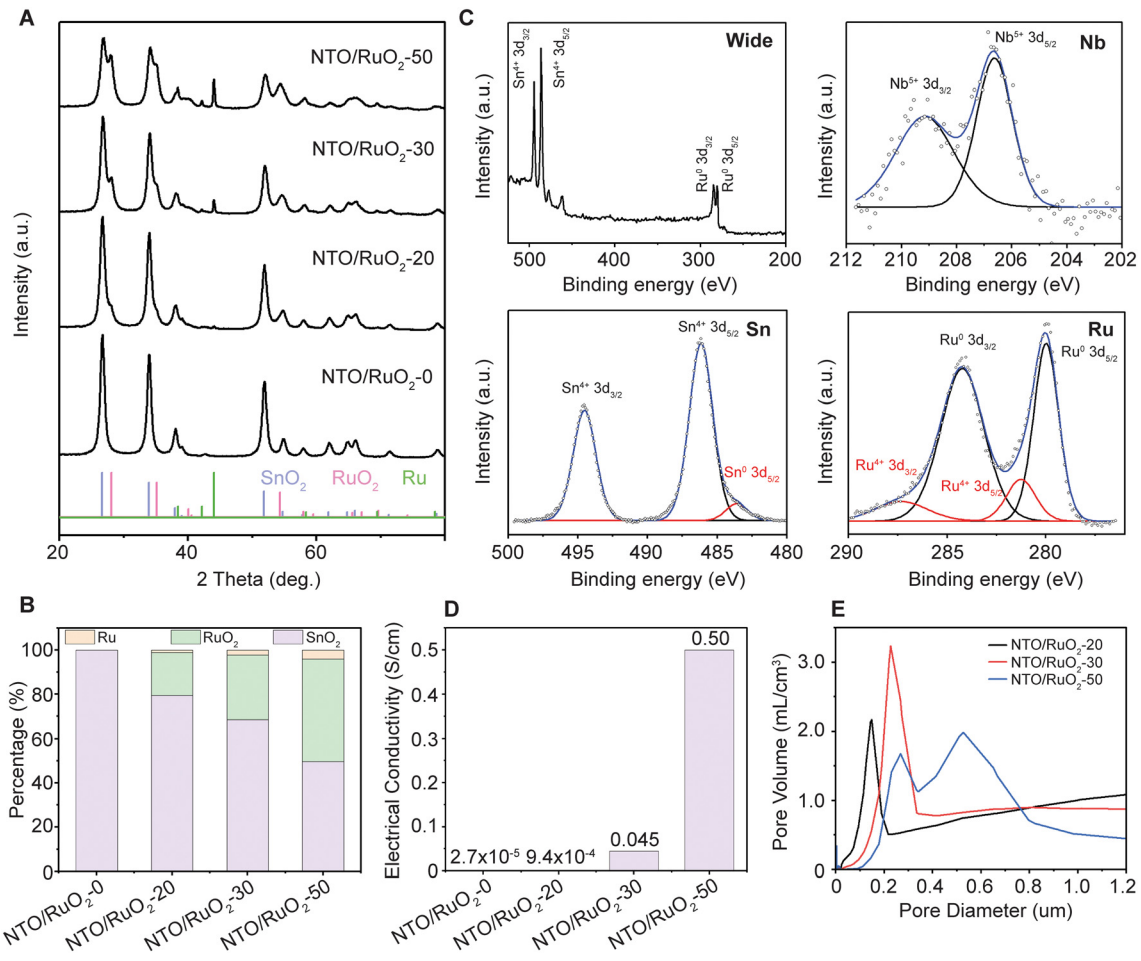

Fig. 2 (A) XRD patterns of macroporous NTO/RuO_2 particles at different RuO_2 binder concentrations, (B) wide, Sn 3d, Ru 3d, and Nb 3d XPS spectra of macroporous NTO/RuO_2-50 particles, (C) percentages of SnO_2, RuO_2, and Ru in macroporous NTO/RuO_2 particles obtained by Rietveld refinements, (D) electrical conductivity of NTO/RuO_2 particles, measured with a compression cell allowing to apply controlled pressures to the powder samples, and (E) pore-size distribution of macroporous NTO/RuO_2 particles measured by a mercury porosimetry method.

© 2025 The Author(s). Published by the Royal Society of Chemistry

Open Access Article. Published on 24 March 2025. Downloaded on 6/13/2026 6:29:26 PM. This article is licensed under a Creative Commons Attribution 3.0 Unported Licence.

contents. In the absence of RuO_2 binder, NTO/RuO_2-0 existed in a tetragonal SnO_2 phase, with characteristic diffraction patterns at 26.6°, 33.9°, 38.0°, and 51.8° (COD 9007533). No Nb species were observed in NTO/RuO_2-0 particles, indicating no precipitation of niobium oxides. With the addition of RuO_2, the XRD patterns of all NTO/RuO_2 particles exhibited diffraction patterns corresponding to the tetragonal SnO_2, tetragonal RuO_2, and metallic Ru phases. Specifically, the diffraction peaks at 28.0°, 35.1°, and 40.1° belonged to the tetragonal phase of RuO_2 (COD 2101852), whereas the peaks at 38.4°, 42.2°, and 44.0° were characteristic of metallic Ru (COD 9008513). The intensities of these RuO_2 and Ru XRD patterns increased as the RuO_2 ratio in the NTO/RuO_2 particles increased. The transformation of $RuCl_3$ salt into RuO_2 initiates in the temperature range of 350–550 °C.[58] Furthermore, RuO_2 decomposes to metallic Ru at a temperature exceeding 1025 °C.[59] Given the high temperature of the flame process (up to approximately 2000 °C),[15] $RuCl_3$ is readily decomposed into RuO_2. Subsequently, RuO_2 can transform to metallic Ru at the high temperature of the flame, and the resulting Ru is oxidized back to RuO_2 in the high-oxygen environment of the flame reactor. Owing to the rapid quenching of the FASP process,[51,60–63] the oxidation of metallic Ru is incomplete, resulting in the presence of a small amount of metallic Ru within the macroporous NTO/RuO_2 particles.

Fig. 2B shows the percentages of SnO_2, RuO_2, and Ru in the macroporous Ru/NTO particles calculated from the XRD patterns. The results imply that the percentages of SnO_2 and total Ru in all macroporous particles were close to the nominal compositions. The crystallographic parameters of RuO_2, Ru, and SnO_2 derived from Rietveld refinement are listed in Table S2.† The refinement was performed using the crystal structure models $P4_2/mnm$ for SnO_2, $P4_2/mnm$ for RuO_2, and $P6_3/mmc$ for Ru. The final *R*-factors indicated the reliability of the analysis. The R_{wp}, R_B, and R_F values were sufficiently low to validate the proposed structural model.

The valance states of Ru, Sn, and Nb in the macroporous NTO/RuO_2-50 particles were determined through XPS measurements, with all peaks calibrated with respect to the C 1s peak at 284.3 eV. As presented in Fig. 2C, the peaks at binding energies of 279.6 eV and 284.8 eV were related to Ru^0 $3d_{5/2}$ and Ru^0 $3d_{3/2}$, respectively. Additionally, the peaks at 280.7 eV and 285.5 eV corresponded to Ru^{4+} $3d_{5/2}$ and Ru^{4+} $3d_{3/2}$, respectively, which were the characteristic peaks of RuO_2. The Sn 3d spectra exhibited peaks at 486.15 eV (Sn^{4+} $3d_{5/2}$), 494.55 eV (Sn^{4+} $3d_{3/2}$), and 483.65 eV (Sn^0 $3d_{5/2}$). The presence of metallic Sn was probably due to the formation of a RuSn alloy in the high-temperature flames of the FASP process and during the post-heat treatment. However, the amount of RuSn alloy was minimal and was not identified in the XRD patterns. The binding energies of Nb 3d were found around 206.65 eV (Nb^{5+} $3d_{5/2}$) and 209.15 eV (Nb^{5+} $3d_{3/2}$), whereas no peaks corresponding to Nb^{3+} or Nb^{4+} were observed. Since the ionic radii of Nb^{5+} (0.64 Å) are smaller than that of Sn^{4+} (0.69 Å), Nb^{5+} ions can be successfully substituted into Sn^{4+} lattice sites, resulting in single-phase NTO nanoparticles with a dopant level of 4 at%.[16,64] The successful substitution of Nb^{5+} enhanced the electrical conductivity of the NTO nanoparticles.[16,64]

The electrical conductivity of the NTO/RuO_2 particles was assessed at various RuO_2 concentrations. It is evident that the porosity of the particles increases the electrical resistance during the direct conductivity measurements of powders. As shown in Fig. 1, the porosity of the macroporous particle determines the framework strength, which is influenced by the varying amounts of RuO_2 binder. To assess the impact of RuO_2 content on the conductivity of the NTO/RuO_2 particles while minimizing the influence of particle porosity on the conductivity measurement, we prepared NTO/RuO_2 aggregate particles without a macroporous structure for conductivity evaluation. The structure of these NTO/RuO_2 aggregate particles is detailed in Fig. S4 in the ESI.† As indicated in Fig. 2D, the electrical conductivity of the NTO aggregate particles was poor (2.7×10^{-5} S cm^{-1}). With the addition of RuO_2 binders, the electrical conductivity of the NTO/RuO_2 particles was noticeably improved. Specifically, as the RuO_2 ratio increased, the electrical conductivity of the NTO/RuO_2 particles increased, reaching 0.50 S cm^{-1} at a RuO_2 content of 50 wt%. It is important to note that RuO_2 exhibits metallic-like conductivity at room temperature with an electrical conductivity of 2.0×10^4 S cm^{-1}.[36] Therefore, combining RuO_2 binders and NTO nanoparticles enhanced the electrical conductivity of the produced NTO/RuO_2 particles. Moreover, at higher RuO_2 concentrations, RuO_2 species precipitated in the gap between NTO nanoparticles and reduce porosity of the framework, as indicated by the TEM and EDS mapping results and the specific surface area of the macroporous NTO/RuO_2 particles. The RuO_2 species in the aggregated NTO particles formed a continuous electrical network, enhancing the conductivity of NTO/RuO_2. Moreover, the reduction in framework porosity at high RuO_2 binder contents not only results in a denser structure but also significantly improves electron transport. The pore size distribution of the macroporous NTO/RuO_2 particles was determined using mercury porosimetry. For NTO/RuO_2-20 particles, the average pore size was 142.6 nm. With an increase in the RuO_2 binder concentration, the peak shifted to a larger pore size, as shown in Fig. 2E, reaching 527.7 nm at a RuO_2 binder content of 50 wt%.

Evaluation of mechanical strength of macroporous particles

As mentioned in the introduction, the macroporous structure has the potential to enhance reactant mass transport, consequently improving the performance of PEFCs. However, in the fabrication process of MEAs, involving mechanical compression, the macroporous framework of particles can be collapsed. To evaluate the mechanical strength of the macroporous structure of NTO/RuO_2 particles, we fabricated MEAs based on the macroporous NTO/RuO_2 particles and used cross-sectional SEM to observe their morphology within

Open Access Article. Published on 24 March 2025. Downloaded on 6/13/2026 6:29:26 PM.
This article is licensed under a Creative Commons Attribution 3.0 Unported Licence.

the MEAs. Fig. 3A shows the fabrication process of MEAs using a direct hot-pressing method. First, macroporous NTO/RuO_2/Teflon was prepared into a square shape (1 cm × 1 cm) and directly hot pressed onto both sides of a Nafion membrane at high pressure of 10 MPa (a typical pressure used for MEA fabrication).[63,65–67] Additionally, another MEA was prepared at a pressure of 40 MPa to gain more insights into the effect of RuO_2 binder on the mechanical strength of the macroporous structure. After hot pressing, the Teflon sheets were removed to obtain a final MEA consisting of a Nafion membrane sandwiched between two macroporous NTO/RuO_2 particle layers. The MEAs were secured using plastic tweezers, immersed in liquid nitrogen for 2 min, removed from liquid nitrogen, and immediately cut using a tweezer needle. The morphology of the particle layer in the MEA was observed using cross-sectional SEM and focused ion beam-SEM (FIB-SEM).

Fig. 3B shows the cross-sectional SEM images of the MEAs based on macroporous NTO/RuO_2 particles and NTO nanoparticles. The MEAs with NTO nanoparticles exhibited low porosity owing to their high compact density. The macroporous NTO/RuO_2-0 particles showed higher porosity compared to that of NTO nanoparticles, and this macroporous structure collapsed at 10 MPa. In contrast, the macropore fraction in the NTO/RuO_2-20 layer was even higher than that in the NTO/RuO_2-0 layer, and the particle structure was nearly broken at a pressure of 10 MPa. Upon further increasing the RuO_2 binder concentration to 50 wt%, the particle structure was maintained at 10 MPa. Interestingly, the macroporous framework of NTO/RuO_2-50 was maintained under the high pressure of 40 MPa, whereas the macroporous NTO/RuO_2-0, NTO/RuO_2-20, and NTO/RuO_2-30 particles were almost broken. These results demonstrated that RuO_2 improved the mechanical strength of the macroporous structure. Additionally, the particle layers fabricated with NTO nanoparticles, NTO/RuO_2-0, NTO/RuO_2-20, NTO/RuO_2-30, and NTO/RuO_2-50, under a pressure of 10 MPa had thicknesses of 7.83, 7.92, 8.08, 8.61, and 8.97 μm, respectively. Higher RuO_2 binder concentration helps to enhance the mechanical strength of macroporous framework of NTO/RuO_2 particles, which maintains the macroporous framework under high pressure. Therefore, using the same particle content and pressure in the MEA fabrication process, an increase in the catalyst layer thickness was observed with an increase in RuO_2 binder contents.

FIB-SEM imaging was employed to gain insights into the pore structure and pore size and to quantitatively assess the

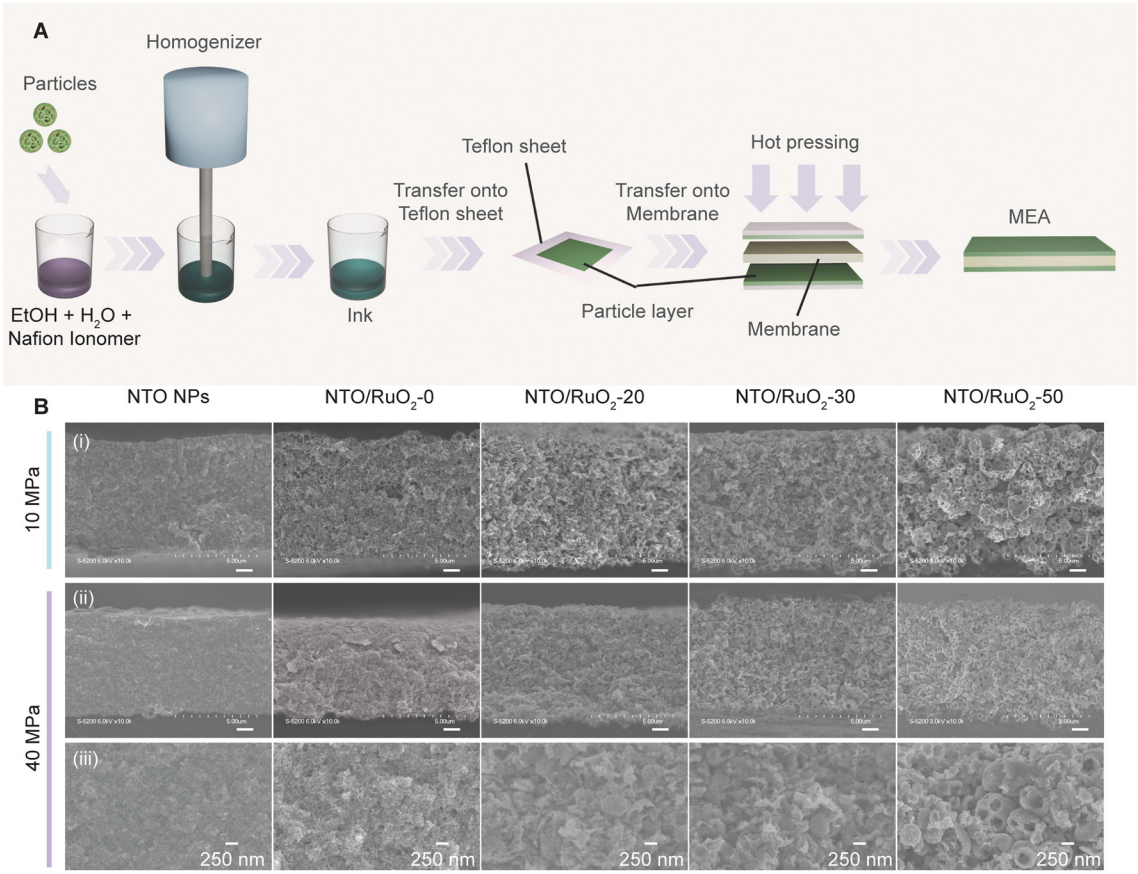

Fig. 3 (A) Schematic of the preparation of an MEA with macroporous NTO/RuO_2 particles. The pressures in the hot-pressing step were 10 MPa and 40 MPa. (B) Cross-sectional SEM images of MEAs using macroporous NTO/RuO_2 particles under pressures of 10 MPa and 40 MPa: (i) low-magnification cross-sectional SEM images under a hot-pressing pressure of 10 MPa, (ii) low-magnification, and (iii) high-magnification cross-sectional SEM images under a hot-pressing pressure of 40 MPa. Bar scale is 1.0 μm.

© 2025 The Author(s). Published by the Royal Society of Chemistry

Open Access Article. Published on 24 March 2025. Downloaded on 6/13/2026 6:29:26 PM.
This article is licensed under a Creative Commons Attribution 3.0 Unported Licence.

porosity of the particle layer in the MEAs. While preparing a cross-section sample through mechanical destruction is straightforward, accurately measuring the porosity can be challenging. In contrast, FIB techniques enable precise cutting of both secondary and primary particles (Fig. 4A), which facilitates the acquisition of more accurate cross-sectional information. The lower- and higher-magnification cross-sectional images of the NTO nanoparticle layer (Fig. 4B and C, respectively) revealed that the NTO nanoparticle layer was dense, with a porosity of 29.1%. Fig. 4D presents the high-magnification cross-sectional FIB-SEM images of the macroporous NTO/RuO_2 particle layers prepared with varying RuO_2 binder concentrations. The porosity of the catalyst layer increases with the amount of RuO_2. For NTO/RuO_2-20, the particle structure almost completely collapsed after compression owing to the low binder content. However, its final remaining porosity was significantly higher than those of the NTO nanoparticles or porous particles without a binder. These results show that RuO_2 binder enhances the mechanical durability of the porous particles and facilitates the formation of robust pores that can withstand the compression process. As the binder content increased, the mechanical stability of the particles improved, which increased the formation of particles that could withstand compression, thereby raising the proportion of remaining PMMA-derived pores. The porosity of the NTO/

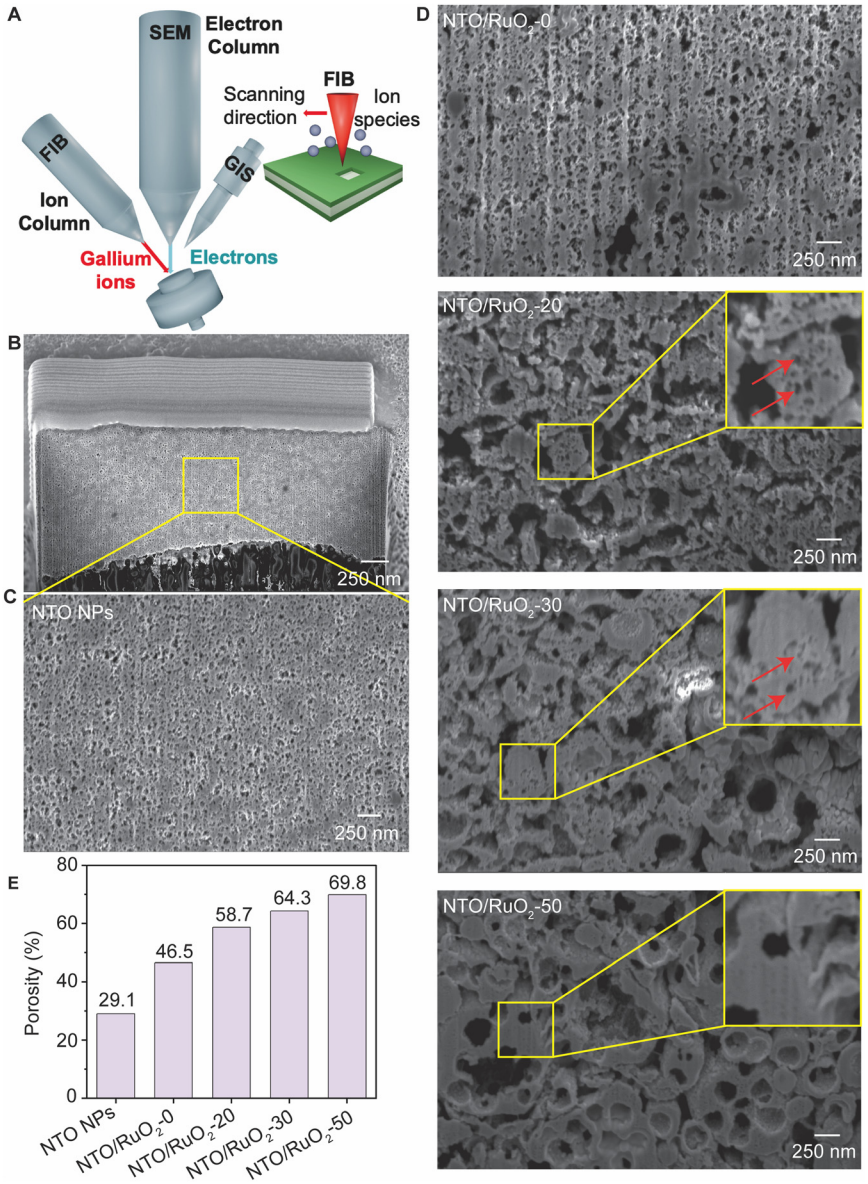

Fig. 4 A) Schematic of FIB-SEM, (B) a low magnification SEM image of a FIB-etched region of NTO nanoparticles, (C) high magnification cross-sectional SEM image of NTO nanoparticles, (D) SEM image of the front face of the cross-section of MEAs using NTO/RuO_2-0, NTO/RuO_2-20, NTO/RuO_2-30, NTO/RuO_2-50 particles under a pressure of 10 MPa, and E) bar graph illustrating the porosity of the particle layer in the MEA fabricated with NTO nanoparticles, NTO/RuO_2-0, NTO/RuO_2-20, NTO/RuO_2-30, NTO/RuO_2-50 particles.

© 2025 The Author(s). Published by the Royal Society of Chemistry

Open Access Article. Published on 24 March 2025. Downloaded on 6/13/2026 6:29:26 PM. This article is licensed under a Creative Commons Attribution 3.0 Unported Licence.

RuO_2-0 layer was 46.5%, which was substantially higher than that of the NTO nanoparticles (29.1%). With the addition of RuO_2 binder, the porosity of the particle layer increased significantly, reaching 69.8% for the macroporous NTO/RuO_2-50 layer, as shown in Fig. 4E, highlighting the beneficial effect of the macroporous structure on enhancing the porosity of the catalyst layer.

Interestingly, the presence of mesopores in the gaps between NTO nanoparticles was also confirmed in the FIB-SEM images. A significant number of mesopores were observed in the NTO/RuO_2-20 layer (red arrow), and the number of mesopores decreased with increasing RuO_2 binder concentration. These mesopores were likely due to the voids between NTO nanoparticles. As discussed previously, the addition of RuO_2 binder reduced the framework porosity of the macroporous NTO/RuO_2 particles. As the concentration of RuO_2 binder gradually increased, the number of mesopores decreased, eventually nearly vanishing for the NTO/RuO_2-50 particles. Specifically, the addition of a large amount of RuO_2 improved the strength of the particle framework and increased the number of macropores derived from the template PMMA within the catalyst layer, while simultaneously diminishing the mesopores between NTO primary particles. Because the balance between the number of mesopores and macropores is essential for improving PEFC performance,[68] the effect of RuO_2 loading on the balance between pore size and PEFC performance will be discussed in the next section.

Performance of MEA using macroporous NTO/RuO_2 particles

To evaluate the practical performance of MEAs with the macroporous NTO/RuO_2 catalyst support, several electrochemical analyses were performed in a single-cell system. MEAs using Carbon Vulcan, NTO nanoparticles, and macroporous NTO/RuO_2 particles at different RuO_2 binder contents were fabricated as catalyst supports for the cathode, as illustrated in Fig. 5A. All MEA tests were conducted in the same operating conditions of 60 °C, 100% RH, and H_2/air. The *I–V* curves of representative MEAs are shown in Fig. 5B. The MEA using Pt/NTO exhibited poorer performance than the MEA using Pt/C in both the low- and high-current-density regions because the low electrical conductivity and porosity of NTO nanoparticles caused ohmic losses and limited mass transport in the catalyst layer. The MEA using macroporous NTO/RuO_2-0 particles showed improved performance compared to that using NTO nanoparticles, with the maximum current density increasing from 1.30 A cm^{-2} to 1.46 A cm^{-2} (as shown in Fig. 5D). The higher porosity of the macroporous NTO/RuO_2-0 particles, compared with that of the NTO nanoparticle layer, decreased gas diffusion resistivity (Fig. 5F) and promoted reactant diffusion to the catalytic sites. No significant differences were observed at a voltage of 0.5 V and in the high-current-density region between the MEAs comprising macroporous NTO/RuO_2 particles and that using commercial Pt/C as a catalyst support (Fig. 5D and E). The MEA using

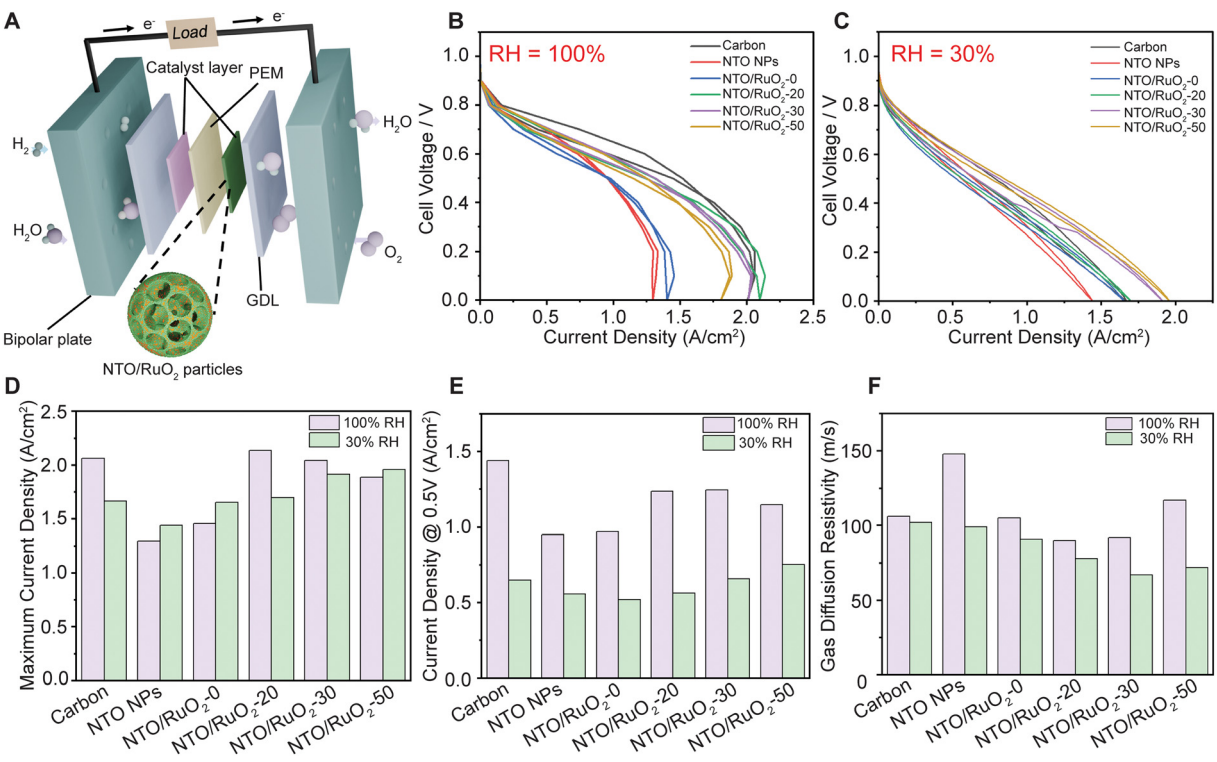

Fig. 5 (A) Schematic of PEFC structures. *I–V* curves of single cell using Carbon Vulcan, NTO nanoparticles, and macroporous NTO/RuO_2 particles at (B) 100% RH, and (C) 30% RH. (D) Bar graph illustrating the maximum current density. (E) Current density at a voltage of 0.5 V. (F) Gas diffusion resistivity of the single cell fabricated with Carbon Vulcan, NTO nanoparticles, and macroporous NTO/RuO_2 particles.

© 2025 The Author(s). Published by the Royal Society of Chemistry

Open Access Article. Published on 24 March 2025. Downloaded on 6/13/2026 6:29:26 PM. This article is licensed under a Creative Commons Attribution 3.0 Unported Licence.

macroporous NTO/RuO_2-20 particles exhibited the best performance, with a maximum current density of 2.16 A cm^{-2}, which is comparable to that using Carbon Vulcan (2.06 A cm^{-2}). This result indicates that the macroporous NTO/RuO_2 particles showed not only high electrical conductivity to avoid an ohmic overpotential but also sufficient porosity for delivering reactants to the catalyst sites. However, the maximum current density decreased when RuO_2 binder content was further increased. The maximum current densities were 2.16 A cm^{-2} and 1.89 A cm^{-2} when macroporous NTO/RuO_2-20 and NTO/RuO_2-50 particles were used as the catalyst supports, respectively. The performance deterioration in the macroporous NTO/RuO_2-50 particles can be attributed to excess water, which obstructs the oxygen transport pathways and reduces the fuel cell efficiency. Water accumulation at the cathode results from both external humidification under high RH conditions and water production from oxygen reduction reaction (ORR),[69] which is accelerated at higher current densities. If the water removal rate does not match the generation rate, excess water can block the pores in the porous cathode catalyst layer, cover the active sites, and clog the gas-transport channels in the flow field.[69,70] For the macroporous NTO/RuO_2 particles, the hydrophilic nature of the RuO_2 binder enhanced the water retention in the catalyst layer, and the high porosity increased oxygen consumption, which resulted in excessive water accumulation and ultimately diminished cell performance. Although the macroporous structure aids in transporting water from the catalyst layer and facilitates water removal through the gas diffusion layer, the increased pore volume can also lead to greater water retention.[69] For the MEA using macroporous NTO/RuO_2-50 particles, a high RuO_2 binder concentration significantly increased the water retention capacity of the catalyst layer. Additionally, the high porosity of the macroporous NTO/RuO_2-50 particles (69.8%) increased the O_2 diffusivity rate, resulting in greater oxygen consumption and higher water generation on the cathode side compared to the macroporous NTO/RuO_2-20 and NTO/RuO_2-30 particles. These factors contribute to more water accumulation and higher gas diffusion resistivity of the MEAs using macroporous NTO/RuO_2-50 particles compared to those using macroporous NTO/RuO_2-20 and NTO/RuO_2-30 particles. Specifically, the gas diffusion resistivity was 90 m s^{-1} for the MEA using macroporous NTO/RuO_2-20 particles and increased to 117 m s^{-1} for that using macroporous NTO/RuO_2-50 particles (Fig. 5F), which explained the deteriorated cell performance.

The amount of RuO_2 binder in the NTO/RuO_2 particles can impact the mechanical strength of the macroporous framework and the wettability of the catalyst layer. A high RuO_2 content is necessary to achieve high electrical conductivity and robust mechanical strength, ensuring that the macroporous framework remains intact under high pressure. However, a high RuO_2 binder content can lead to water accumulation in the MEAs under fully humidified conditions and degrade cell performance. Therefore, optimizing the amount of RuO_2 binder is essential to achieve a catalyst layer that maintains structural integrity and high conductivity without compromising performance owing to water accumulation.

We also evaluated the performance of these MEAs at low RH of 30% and a high temperature of 80 °C. Theoretically, in the case of limited external humidification, the water used to humidify the MEA is primarily supplied by the water produced from the ORR at the cathode. Given the limited water content under low RH, the conductivity drops, leading to increased ionic resistance and ohmic losses, ultimately degrading the performance.[70–72] The *I–V* curves of the MEAs using Carbon Vulcan, NTO nanoparticles, and macroporous NTO/RuO_2 particles as cathode catalyst supports are shown in Fig. 5C. Compared to those at 100% RH, the ohmic resistance at 30% RH increased for all MEAs, resulting in a drop in current density at 0.5 V. The maximum current density of the MEA using Carbon Vulcan as a catalyst support decreased from 2.06 A cm^{-2} to 1.67 A cm^{-2}, primarily due to the hydrophobic nature of carbon, which fails to maintain necessary humidity within the catalyst layer and results in increased ohmic and mass transfer resistance. Conversely, MEAs utilizing NTO nanoparticles and macroporous NTO/RuO_2-0 particles exhibited sustained performance. This can be attributed to the hydrophilic properties of SnO_2, which help maintain membrane hydration and overall cell performance under low-humidification conditions. With an increase in the RuO_2 binder content, the maximum current density at 30% RH gradually increased. This trend can be attributed to the increased water production at the cathode, which improved the hydration status of the MEA. The hydrophilic nature of the RuO_2 binder enhanced the water retention capability at the catalyst layer/membrane interface, thereby improving membrane hydration and overall cell performance.

To assess the durability of macroporous NTO/RuO_2 particles, cyclic voltammograms (CV) were obtained for electrodes based on macroporous NTO/RuO_2 particles with varying RuO_2 binder contents, NTO nanoparticles, and commercial carbon, both before and after testing at an applied potential of 1.3 V *vs.* $E_{Ag/AgCl}$ for 10 minutes, as shown in Fig. S7.† The results reveal that the carbon support exhibited a significant increase in capacitance after the durability test, suggesting carbon oxidation and degradation occurred. In contrast, no change in the CV shape was observed for NTO nanoparticles and macroporous NTO/RuO_2 particles, indicating their high stability after the durability test at high potential. Hence, compared to carbon, which is the conventional catalyst support for PEFCs, macroporous NTO/RuO_2 particles show significant promise as potential cathode catalyst supports, providing both excellent performance and durability for PEFCs.

Conclusions

Macroporous NTO/RuO_2 particles with high mechanical strengths and electrical conductivities were successfully synthesized *via* flame-assisted spray pyrolysis. The effects of

Open Access Article. Published on 24 March 2025. Downloaded on 6/13/2026 6:29:26 PM. This article is licensed under a Creative Commons Attribution 3.0 Unported Licence.

RuO_2 binder and PMMA template concentrations on the structure and morphology of the macroporous NTO/RuO_2 particles were investigated. The macroporous NTO/RuO_2 particles have a spherical shape, with the gap between NTO nanoparticles filled with RuO_2 particles, leading to a decreased framework porosity. The electrical conductivity of the NTO/RuO_2 particles increased with RuO_2 binder content, reaching 0.50 S cm^{-1} at 50 wt% RuO_2. The macroporous structure of the NTO/RuO_2-50 particles remained stable at 40 MPa, demonstrating that the RuO_2 binder improved the mechanical strength of the macroporous framework. The porosity of the catalyst layer increased from 29.1% for NTO/RuO_2-0 to 69.8% for NTO/RuO_2-50. The performance of the MEAs using macroporous NTO/RuO_2-20 particles was comparable to that of the MEAs using a Carbon Vulcan catalyst support under high RH conditions. Additionally, the hydrophilic nature of RuO_2 binders enhanced the overall cell performance when operated at low RH. These findings highlight that incorporating RuO_2 as a binder not only enhances the mechanical strength of the macroporous framework but also improves its PEFC performance, demonstrating that macroporous NTO/RuO_2 particles are promising candidates as cathode catalyst supports in PEFCs.

Experimental section

Particle synthesis

The procedure for producing NTO nanoparticles has been described in detail in a previous study.[18] Briefly, NTO nanoparticles were synthesized *via* flame spray pyrolysis (FSP). The precursor solutions, including $Sn(O_2C_8H_{15})_2$ (92.5–100%, Sigma-Aldrich) and $Nb(OC_2H_5)_5$ (99.95% purity, Sigma-Aldrich), were dissolved in xylene. The total Sn and Nb concentration was 0.1 mol L^{-1} with a Nb dopant content of 4 at%. The precursor solution was introduced into a two-fluid nozzle (AM6, ATOMAX Co., Ltd., Shizuoka, Japan) at 3.0 mL min^{-1} using a syringe pump. This solution was atomized with oxygen (3.0 L min^{-1}) and ignited by a premixed methane/air pilot flame (CH_4: 1.5 L min^{-1}, air: 11.0 L min^{-1}). NTO nanoparticles were collected using a polytetrafluoroethylene (PTFE) membrane filter (HORKOS Corp., Hiroshima, Japan). NTO nanoparticles were used as the precursors for the synthesis of macroporous NTO/RuO_2 particles.

The macroporous NTO/RuO_2 particles were prepared by the flame method using a precursor solution containing flame-made NTO nanoparticles, $RuCl_3{\cdot}xH_2O$ (99.9%, Wako, Japan) and poly(methyl methacrylate) (PMMA) (MP-2741, Soken, Japan) as a template. The solution in a round bottom flask was placed in a circulating water-cooling system to maintain the stability of the precursors. The RuO_2/(NTO + RuO_2) mass ratios were controlled at 0, 20, 30 and 50 wt%. The concentration of PMMA template in the precursor was 1.0 wt%. An ultrasonic nebulizer (NE-U17, Omron Healthcare Co., Ltd., Tokyo, Japan) was used to create droplets from the precursor solution. The generated droplets were introduced into diffusion flames using nitrogen as a carrier gas at a flow rate of 5.0 L min^{-1}. A diffusion flame was formed using methane (0.5 L min^{-1}) as a fuel and oxygen (1.3 L min^{-1}) as an oxidizer. The macroporous NTO/RuO_2 particles were collected using a PTFE membrane filter. Then, the macroporous NTO/RuO_2 particles were placed in a tubular furnace and heated from room temperature to 500 °C at a heating rate of 10 °C min^{-1} under air conditions. The temperature was held for 60 min to remove PMMA completely. The obtained particles are denoted as NTO/RuO_2-*x*, where *x* refers to the percentage of the RuO_2 binder in the particles. For example, NTO/RuO_2-20 is a macroporous NTO/RuO_2 particle containing 20 wt% RuO_2 binder, as calculated from the precursor used.

To investigate the effect of PMMA concentration on the morphology and macroporous structure of the NTO/RuO_2 particles, the PMMA content in the precursor was changed from 0, 0.5, 1.0, to 2.0 wt%. The concentration of RuO_2 binder was fixed at 50 wt%. The particles were also produced using FASP under the same conditions. The synthesized particles underwent a heat treatment at 500 °C for 1 h under air conditions to remove PMMA completely.

Characterization

The crystal structures of the macroporous NTO/RuO_2 particles were examined by X-ray diffraction (XRD; D2 PHASER, 40 kV and 30 mA, Bruker Corp., USA). The size, morphology, and structure of the particles were characterized by field-emission scanning electron microscopy (FE-SEM; S-5200, Hitachi High-Tech. Corp., Tokyo, Japan). The electrical conductivities of the aggregated NTO/RuO_2 particles were measured using a multi-electrochemical measurement system (HZ-Pro S4, Hokuto Denko, Japan). The oxidation states of the elements were determined using X-ray photoelectron spectroscopy (XPS, ESCA-3400, Shimadzu Corp.) operated at 10 kV and 20 mA.

The mechanical strength of the macroporous structure of the NTO/RuO_2 particles was evaluated at different compression pressures during MEA fabrication. The ink was prepared by dispersing 0.5 g of macroporous NTO/RuO_2 particles in a mixed solvent containing 0.405 g of 20 wt% Nafion solution (Wako, Japan), 0.661 g of ethanol, and 0.808 g of deionized water and ultrasonicating for 60 min. The as-prepared catalyst ink (0.5 mL) was then applied to a Teflon sheet. An electrolyte membrane (DuPont, NR-212) was sandwiched between two sheets of macroporous NTO/RuO_2 and assembled by hot pressing (Mini Test Press MP, Toyo Seiki Co., Ltd.) at 126 °C with pressures of 10 and 40 MPa. The morphology of the macroporous NTO/RuO_2 particle layers in the MEA was observed by cross-sectional SEM and focused ion beam-SEM (FIB-SEM; HeliosG4 UC, Thermo Fisher Scientific, Waltham, MA, USA). The pore-size distribution of the macroporous NTO/RuO_2 particles was measured using mercury porosimetry.

The MEA showed enhanced performance when macroporous NTO/RuO_2 particles were used as the cathode catalyst support.

© 2025 The Author(s). Published by the Royal Society of Chemistry

Open Access Article. Published on 24 March 2025. Downloaded on 6/13/2026 6:29:26 PM. This article is licensed under a Creative Commons Attribution 3.0 Unported Licence.

The MEA preparation process was described in detail in a previous study.[32] Briefly, cathode catalyst inks were prepared by mixing a specific amount of Pt/(NTO/RuO_2) or Pt/(NTO) catalyst, Nafion ionomers, ethanol, and purified water using a homogenizer to achieve an ionomer/support (*I*/*S*) volume ratio of 0.175. The catalyst ink was then applied to a Teflon sheet with a Pt loading of 0.1 mg cm^{-2}. For the anode, Pt/C (with 20 wt% Pt from Ketjenblack ECP) was used in all test cells. The Pt loading was ~0.1 mg cm^{-2}, and the *I*/*S* ratio was ~1.0. For comparison, commercial Pt/C (XC-72R, Cabot Corporation) was used as a reference cathode catalyst at the same Pt loading. Pt/(NTO/RuO_2), comprising an electrolyte membrane (DuPont, NR-212) and a Pt/C sheet, was assembled by hot pressing at 10 MPa and 126 °C. Each electrode has a geometric area of 1.0 cm^2. The MEA was placed in a custom single-cell holder with straight-line gas-flow channels. The output performance was evaluated by recording the current density at 60 °C and 100% RH, and at 80 °C and 30% RH. Hydrogen gas was supplied to the anode, and air was supplied to the cathode, both with a backpressure of 108 kPa. Gas flow rates were 1.0 L min^{-1} and 0.5 L min^{-1} at the cathode and anode, respectively. A pre-conditioning process (40 cycles at 0.1 V s^{-1} over 0–1.0 V) was completed before the main measurements. AC-impedance measurements were conducted from 100 kHz to 0.1 Hz at a potential of 0.4 V and an amplitude of 0.02 V. The cells and MEAs used for the AC-impedance measurements were identical to those used for the output measurements, and the experimental conditions were also identical. Current–voltage curves were measured potentiostatically at 0.01 V s^{-1} in the range of 0–1.0 V.

The durability of carbon, NTO nanoparticles, and macroporous NTO/RuO_2 particles with varying RuO_2 binder contents was evaluated through chronoamperometry by applying a voltage of 1.3 V *versus* Ag/AgCl. Their electrochemical properties, both before and after the durability test, were assessed using cyclic voltammetry (CV) with a potentiostat (HZ-5000, Hokuto Denko Corp., Tokyo, Japan) at a scan rate of 20 mV s^{-1} in nitrogen-saturated 0.1 N $HClO_4$ solution. The electrode potential *versus* Ag/AgCl ($E_{Ag/AgCl}$) was converted to the potential *versus* a reversible hydrogen electrode (E_{RHE}) using the Nernst equation: $E_{RHE} = E_{Ag/AgCl} + 0.059\ pH + 0.198$.

Data availability

The data supporting this article have been included as part of the ESI.†

Author contributions

Thi Thanh Nguyen Ho: writing – original draft, writing – review & editing, validation, investigation, data curation, visualization. Tomoyuki Hirano: conceptualization, writing – review & editing, supervision, funding acquisition. Aoi Takano: investigation, data curation, writing – review & editing. Syu Miyasaka: investigation, data curation, writing – review & editing. Eishi Tanabe: investigation, data curation, writing – review & editing. Makoto Maeda: investigation, data curation, writing – review & editing. Eka Lutfi Septiani: writing – review & editing, investigation. Kiet Le Anh Cao: writing – review & editing, investigation. Takashi Ogi: conceptualization, writing – review & editing, supervision, funding acquisition.

Conflicts of interest

There are no conflicts to declare.

Acknowledgements

This work was supported by JSPS KAKENHI Grant No. JP22K20482, JP23K13590 (T. H.), and JP23H01745 (T. O.). This work was supported by the JST SPRING, Grant Number JPMJSP2132 (T. T. N. H.). This work was partially supported by the Center for Functional Nano Oxides at Hiroshima University, the Information Center of Particle Technology, Japan, and the Hosokawa Powder Technology Foundation. The authors thank the Natural Science Center for Basic Research and Development (N-BARD) for access to SEM facilities.

References

1 N. Seselj, S. M. Alfaro, E. Bompolaki, L. N. Cleemann, T. Torres and K. Azizi, *Adv. Mater.*, 2023, **35**, 2302207.
2 S. Jang, Y. S. Kang, D. Kim, S. Park, C. Seol, S. Lee, S. M. Kim and S. J. Yoo, *Adv. Mater.*, 2023, **35**, 2204902.
3 F. Ning, J. Qin, X. Dan, S. Pan, C. Bai, M. Shen, Y. Li, X. Fu, S. Zhou, Y. Shen, W. Feng, Y. Zou, Y. Cui, Y. Song and X. Zhou, *ACS Nano*, 2023, **17**, 9487–9500.
4 B. Yang, Q. Han, L. Han, Y. Leng, T. O'Carroll, X. Yang, G. Wu and Z. Xiang, *Adv. Mater.*, 2023, **35**, 2208661.
5 D. A. Cullen, K. C. Neyerlin, R. K. Ahluwalia, R. Mukundan, K. L. More, R. L. Borup, A. Z. Weber, D. J. Myers and A. Kusoglu, *Nat. Energy*, 2021, **6**, 462–474.
6 K. Khedekar, A. Zaffora, M. Santamaria, M. Coats, S. Pylypenko, J. Braaten, P. Atanassov, N. Tamura, L. Cheng, C. Johnston and I. V. Zenyuk, *Nat. Catal.*, 2023, **6**, 676–686.
7 S. Komini Babu, R. Mukundan, C. Wang, D. Langlois, D. A. Cullen, D. Papadias, K. L. More, R. Ahluwalia, J. Waldecker and R. Borup, *J. Electrochem. Soc.*, 2021, **168**, 044502.
8 J. D. Sinniah, W. Y. Wong, K. S. Loh, R. M. Yunus and S. N. Timmiati, *J. Power Sources*, 2022, **534**, 231422.
9 E. Antolini, *Appl. Catal., B*, 2009, **88**, 1–24.
10 Y. J. Wang, B. Fang, H. Li, X. T. Bi and H. Wang, *Prog. Mater. Sci.*, 2016, **82**, 445–498.
11 A. Kumar, E. J. Park, Y. S. Kim and J. S. Spendelow, *Macromol. Chem. Phys.*, 2024, **225**, 2400092.
12 T. T. N. Ho, T. Hirano, R. Narui, H. Tsutsumi, M. Kishi, Y. Yoshikawa, K. L. A. Cao and T. Ogi, *Adv. Powder Technol.*, 2024, **35**, 104568.
13 Y. Takabatake, Z. Noda, S. M. Lyth, A. Hayashi and K. Sasaki, *Int. J. Hydrogen Energy*, 2014, **39**, 5074–5082.
14 T. Ikehara, Z. Noda, J. Matsuda, M. Nishihara, A. Hayashi and K. Sasaki, *ECS Trans.*, 2020, **98**, 573–582.

Open Access Article. Published on 24 March 2025. Downloaded on 6/13/2026 6:29:26 PM. This article is licensed under a Creative Commons Attribution 3.0 Unported Licence.

15 T. T. N. Ho, T. Hirano, R. Narui, H. Tsutsumi, M. Kishi, Y. Yoshikawa, K. L. A. Cao and T. Ogi, *ACS Appl. Energy Mater.*, 2023, **6**, 6064–6071.
16 Y. Senoo, K. Kakinuma, M. Uchida, H. Uchida, S. Deki and M. Watanabe, *RSC Adv.*, 2014, **4**, 32180–32188.
17 T. Hirano, T. Tsuboi, K. L. A. Cao, E. Tanabe and T. Ogi, *J. Nanopart. Res.*, 2022, **25**, 1.
18 T. Hirano, T. Tsuboi, E. Tanabe and T. Ogi, *J. Alloys Compd.*, 2022, **898**, 162749.
19 T. Hirano, T. Tsuboi, T. T. N. Ho, E. Tanabe, A. Takano, M. Kataoka and T. Ogi, *ACS Appl. Energy Mater.*, 2023, **6**, 12364–12370.
20 P. H. Le, K. L. A. Cao, Y. Kitamoto, T. Hirano and T. Ogi, *Langmuir*, 2023, **39**, 7783–7792.
21 P. H. Le, Y. Kitamoto, S. Yamashita, K. L. A. Cao, T. Hirano, T. W. M. Amen, N. Tsunoji and T. Ogi, *ACS Appl. Mater. Interfaces*, 2023, **15**, 54073–54084.
22 D. B. Kautsar, P. H. Le, A. Ando, K. L. A. Cao, E. L. Septiani, T. Hirano and T. Ogi, *Langmuir*, 2024, **40**, 8260–8270.
23 T. T. Nguyen, M. Miyauchi, A. M. Rahmatika, K. L. A. Cao, E. Tanabe and T. Ogi, *ACS Appl. Mater. Interfaces*, 2022, **14**, 14435–14446.
24 T. T. Nguyen, A. M. Rahmatika, M. Miyauchi, K. L. A. Cao and T. Ogi, *Langmuir*, 2021, **37**, 4256–4266.
25 T. T. Nguyen, N. S. N. Saipul Bahri, A. M. Rahmatika, K. L. A. Cao, T. Hirano and T. Ogi, *ACS Appl. Bio Mater.*, 2023, **6**, 2725–2737.
26 S. Wintzheimer, L. Luthardt, K. L. A. Cao, I. Imaz, D. Maspoch, T. Ogi, A. Bück, D. P. Debecker, M. Faustini and K. Mandel, *Adv. Mater.*, 2023, **35**, 2306648.
27 T. Ogi, A. B. D. Nandiyanto and K. Okuyama, *Adv. Powder Technol.*, 2014, **25**, 3–17.
28 M. Faustini, M. Giraud, D. Jones, J. Rozière, M. Dupont, T. R. Porter, S. Nowak, M. Bahri, O. Ersen, C. Sanchez, C. Boissière, C. Tard and J. Peron, *Adv. Energy Mater.*, 2019, **9**, 1802136.
29 T. Van Pham, T. Hirano, K. L. A. Cao, E. L. Septiani, E. Tanabe and T. Ogi, *Energy Fuels*, 2024, **38**, 16743–16755.
30 P. H. Le, Y. Kitamoto, K. L. A. Cao, T. Hirano, E. Tanabe and T. Ogi, *Adv. Powder Technol.*, 2022, **33**, 103581.
31 P. H. Le, S. Yamashita, K. L. A. Cao, T. Hirano, N. Tsunoji, D. B. Kautsar and T. Ogi, *ACS Appl. Nano Mater.*, 2023, **6**, 17324–17335.
32 T. Hirano, T. Tsuboi, T. T. N. Ho, E. Tanabe, A. Takano, M. Kataoka and T. Ogi, *Nano Lett.*, 2024, **24**, 10426–10433.
33 A. Shimamura, M. Fukushima, M. Hotta, T. Ohji and N. Kondo, *J. Am. Ceram. Soc.*, 2016, **99**, 440–444.
34 A. N. Chen, J. Y. Chen, J. M. Wu, L. J. Cheng, R. Z. Liu, J. Liu, Y. Chen, C. H. Li, S. F. Wen and Y. S. Shi, *Ceram. Int.*, 2019, **45**, 21136–21143.
35 Y. Huang, D. Dong, J. Yao, L. He, J. Ho, C. Kong, A. J. Hill and H. Wang, *Chem. Mater.*, 2010, **22**, 5271–5278.
36 Y. Lee, B.-U. Ye, H. k. Yu, J.-L. Lee, M. H. Kim and J. M. Baik, *J. Phys. Chem. C*, 2011, **115**, 4611–4615.
37 A. S. Hassan, K. Moyer, B. R. Ramachandran and C. D. Wick, *J. Phys. Chem. C*, 2016, **120**, 2036–2046.
38 X. Wu, J. Tayal, S. Basu and K. Scott, *Int. J. Hydrogen Energy*, 2011, **36**, 14796–14804.
39 J. Y. Lim, G. Rahman, S. Y. Chae, K.-Y. Lee, C.-S. Kim and O.-S. Joo, *Int. J. Energy Res.*, 2014, **38**, 875–883.
40 R. Balgis, A. F. Arif, T. Mori, T. Ogi, K. Okuyama and G. M. Anilkumar, *AIChE J.*, 2016, **62**, 440–450.
41 R. Strobel and S. E. Pratsinis, *J. Mater. Chem.*, 2007, **17**, 4743–4756.
42 L. Gradon, R. Balgis, T. Hirano, A. M. Rahmatika, T. Ogi and K. Okuyama, *J. Aerosol Sci.*, 2020, **149**, 105608.
43 L. Mädler, H. K. Kammler, R. Mueller and S. E. Pratsinis, *J. Aerosol Sci.*, 2002, **33**, 369–389.
44 T. Hirano, S. Kaseda, K. Le Anh Cao, F. Iskandar, E. Tanabe and T. Ogi, *ACS Appl. Nano Mater.*, 2022, **5**, 15449–15456.
45 K. L. A. Cao, Y. Kito, P. H. Le, T. Ogi and T. Hirano, *ACS Appl. Eng. Mater.*, 2023, **1**, 1789–1798.
46 M. Ismael, A. Sharma and N. Kumar, *Sustainable Mater. Technol.*, 2024, **40**, e00826.
47 T. Hirano, J. Kikkawa, F. G. Rinaldi, K. Kitawaki, D. Shimokuri, E. Tanabe and T. Ogi, *Ind. Eng. Chem. Res.*, 2019, **58**, 7193–7199.
48 T. Hirano, J. Kikkawa, D. Shimokuri, A. B. D. Nandiyanto and T. Ogi, *J. Chem. Eng. Jpn.*, 2021, **54**, 557–565.
49 K. Wegner, B. Schimmöller, B. Thiebaut, C. Fernandez and T. N. Rao, *Kona Powder Part. J.*, 2011, **29**, 251–265.
50 H. K. Kammler, L. Mädler and S. E. Pratsinis, *Chem. Eng. Technol.*, 2001, **24**, 583–596.
51 W. Y. Teoh, R. Amal and L. Mädler, *Nanoscale*, 2010, **2**, 1324–1347.
52 N. E. Motl, A. K. P. Mann and S. E. Skrabalak, *J. Mater. Chem. A*, 2013, **1**, 5193–5202.
53 R. Strobel, A. Baiker and S. E. Pratsinis, *Adv. Powder Technol.*, 2006, **17**, 457–480.
54 H. Wu, T. Yildirim and W. Zhou, *J. Phys. Chem. Lett.*, 2013, **4**, 925–930.
55 M. Inaba, R. Murase, T. Takeshita, K. Yano, S. Kosaka, N. Takahashi, N. Isomura, K. Oh-ishi, W. Yoshimune, K. Tsuchiya, T. Nobukawa and K. Kodama, *ACS Appl. Mater. Interfaces*, 2024, **16**, 10295–10306.
56 H. Lee, P. R. Deshmukh, J. H. Kim, H. S. Hyun, Y. Sohn and W. G. Shin, *J. Alloys Compd.*, 2019, **810**, 151923.
57 A. B. D. Nandiyanto, N. Hagura, F. Iskandar and K. Okuyama, *Acta Mater.*, 2010, **58**, 282–289.
58 C. Malmgren, A. K. Eriksson, A. Cornell, J. Bäckström, S. Eriksson and H. Olin, *Thin Solid Films*, 2010, **518**, 3615–3618.
59 R. G. Vadimsky, R. P. Frankenthal and D. E. Thompson, *J. Electrochem. Soc.*, 1979, **126**, 2017–2023.
60 A. Purwanto, W.-N. Wang, I. W. Lenggoro and K. Okuyama, *J. Electrochem. Soc.*, 2007, **154**, J91.
61 T. Hirano, N. Kadowaki, A. Ichimiya, R. Narui and T. Ogi, *Sci. Technol. Energ. Mater.*, 2023, **84**, 40–44.
62 S. Nakakura, A. F. Arif, F. G. Rinaldi, T. Hirano, E. Tanabe, R. Balgis and T. Ogi, *Adv. Powder Technol.*, 2019, **30**, 6–12.
63 T. Pinheiro Araújo, J. Morales-Vidal, T. Zou, R. García-Muelas, P. O. Willi, K. M. Engel, O. V. Safonova, D. Faust

© 2025 The Author(s). Published by the Royal Society of Chemistry

Akl, F. Krumeich, R. N. Grass, C. Mondelli, N. López and J. Pérez-Ramírez, *Adv. Energy Mater.*, 2022, **12**, 2103707.
64 R. Ramarajan, M. Kovendhan, K. Thangaraju and D. P. Joseph, *Ceram. Int.*, 2020, **46**, 12224–12231.
65 M. Chisaka, *J. Mater. Chem. A*, 2024, **12**, 18636–18673.
66 N. Narischat, T. Takeguchi, T. Tsuchiya, T. Mori, I. Ogino, S. R. Mukai and W. Ueda, *J. Phys. Chem. C*, 2014, **118**, 23003–23010.
67 A. Lindermeir, G. Rosenthal, U. Kunz and U. Hoffmann, *Fuel Cells*, 2004, **4**, 78–85.
68 T. Gu, R. Shi, J. Guo, W. Wang, X. Wei, Q. Zhang, J. Luo and R. Yang, *Energy Fuels*, 2024, **38**, 15714–15720.
69 H. Li, Y. Tang, Z. Wang, Z. Shi, S. Wu, D. Song, J. Zhang, K. Fatih, J. Zhang, H. Wang, Z. Liu, R. Abouatallah and A. Mazza, *J. Power Sources*, 2008, **178**, 103–117.
70 W. Schmittinger and A. Vahidi, *J. Power Sources*, 2008, **180**, 1–14.
71 J.-M. Le Canut, R. M. Abouatallah and D. A. Harrington, *J. Electrochem. Soc.*, 2006, **153**, A857.
72 Y. Sone, P. Ekdunge and D. Simonsson, *J. Electrochem. Soc.*, 1996, **143**, 1254.

Open Access Article. Published on 24 March 2025. Downloaded on 6/13/2026 6:29:26 PM.
This article is licensed under a Creative Commons Attribution 3.0 Unported Licence.